Hindawi Publishing Corporation
Journal of Nanomaterials
Volume 2012, Article ID 524343, 17 pages
doi:10.1155/2012/524343

Research Article

The Effect of Film Thickness and TiO_2 Content on Film Formation from PS/TiO_2 Nanocomposites Prepared by Dip-Coating Method

M. Selin Sunay,[1] Onder Pekcan,[2] and Saziye Ugur[1]

[1] *Department of Physics, Istanbul Technical University, Maslak, 34469 Istanbul, Turkey*
[2] *Kadir Has University, Cibali, 34320 Istanbul, Turkey*

Correspondence should be addressed to Saziye Ugur, brbaban@hotmail.com

Received 28 January 2012; Accepted 12 March 2012

Academic Editor: Sevan P. Davtyan

Steady-state fluorescence (SSF) technique in conjunction with UV-visible (UVV) technique and atomic force microscope (AFM) was used for studying film formation from TiO_2 covered nanosized polystyrene (PS) latex particles (320 nm). The effects of film thickness and TiO_2 content on the film formation and structure properties of PS/TiO_2 composites were studied. For this purpose, two different sets of PS films with thicknesses of 5 and 20 μm were prepared from pyrene-(P-) labeled PS particles and covered with various layers of TiO_2 using dip-coating method. These films were then annealed at elevated temperatures above glass transition temperature (T_g) of PS in the range of 100–280°C. Fluorescence emission intensity, I_p from P and transmitted light intensity, I_{tr} were measured after each annealing step to monitor the stages of film formation. The results showed that film formation from PS latexes occurs on the top surface of PS/TiO_2 composites and thus developed independent of TiO_2 content for both film sets. But the surface morphology of the films was found to vary with both TiO_2 content and film thickness. After removal of PS, thin films provide a quite ordered porous structure while thick films showed nonporous structure.

1. Introduction

As a result of worldwide efforts by theorists and experimentalists, a very good understanding of the mechanisms of latex film formation has been achieved [1]. During film formation polymer lattices undergo an irreversible change from a stable colloidal dispersion to a continuous, transparent, and mechanically stable film [1–6]. The process of film formation is usually divided into three stages: (i) water evaporation and subsequent packing of polymer particles; (ii) deformation of the particles and close contact between the particles if their glass transition temperature (T_g) is less than or close to the drying temperature (soft or low T_g latex). Latex with a T_g above the drying temperature (hard or high T_g latex) stays undeformed at this stage. In the annealing of a hard latex system, deformation of particles first leads to void closure [2–4] and then after the voids disappear, diffusion across particle-particle boundaries starts, that is, the mechanical properties of hard latex films evolve during annealing, after all solvent has evaporated and all voids have disappeared. (iii) Coalescence of the deformed particles to form a homogeneous film [3] where macromolecules belonging to different particles mix by interdiffusion [5, 6]. This understanding of latex film formation can now be exploited to underpin the processing of new types of coatings and development of new materials. The blending of latex particles and inorganic nanoparticles provides a facile means of ensuring dispersion at the nanometer scale in composite coatings.

Over the past decades, porous materials have attracted increasing interest owing to their potential applications in the fields of catalysis, ion exchange, adsorption, and separation [7, 8]. Since the successful preparation of ordered mesoporous silicas [9], a great deal of progress has been made in the synthesis of ordered microporous (pore size below 2 nm), mesoporous (2–50 nm), and macroporous (beyond 50 nm) materials [10, 11]. Latex spheres can be used as templates to form ordered macroporous materials [12, 13]. The assembly of colloidal particles has attracted a great deal of attention from both the theoretical and experimental aspects. Colloidal crystals consisting of three-dimensional ordered arrays of monodispersed spheres, represent novel

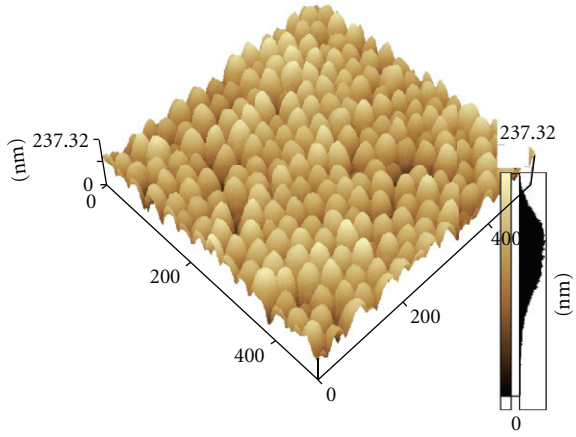

Figure 1: AFM image of polystyrene latex (320 nm) used in this study.

templates for the preparation of highly ordered macroporous inorganic solids, exhibiting precisely controlled pore sizes and highly ordered three-dimensional porous structures. This macroscale templating approach typically consists of three steps. First, the interstitial voids of the monodisperse sphere arrays are filled with precursors of various classes of materials, such as ceramics, semiconductors, metals, and monomers. In the second step, the precursors condense and form a solid framework around the spheres. Finally, the spheres are removed by either calcination or solvent extraction.

The colloidal crystal templates used to prepare three-dimensional macroporous materials include monodisperse polystyrene (PS), poly(methyl methacrylate) (PMMA), and silica spheres. The ability to control wall thickness, pore size, elemental and phase compositions makes the colloidal sphere array templating a versatile, attractive, and flexible route for the synthesis of highly ordered macroporous materials with fine-tuned pore and framework architectures. The PS colloid beads are usually considered as small solid particles with at least one characteristic dimension in the range of a few tens of nanometers to one micrometer. The combination of surfactant and colloidal crystal templating methods offers an efficient way for the construction of ordered and interconnected micro- macro-, mesomacroporous architectures [14–17]. Colloidal latex spheres, all having the same diameter, can be self-aggregated in a regular fashion, then the mixture of the inorganic precursors and surfactant (or copolymer) micellar solution is allowed to infiltrate the interstitial spaces between the spheres. This is followed by condensation and crystallization of the inorganic precursors. The removal of the surfactant and latex spheres, by either high-temperature calcination or solvent extraction, leads to the formation of 3D ordered micro- macro- or mesomacroporous materials. The wall thickness of macroporous structures can be controlled by the hydrolysis/condensation rates of the inorganic precursors [18], the PS spheres packing [19] and by forming core-shell structures at the sphere surface (i.e., deposition of polyelectrolyte multilayers at the sphere surface) [20]. The pore size can be easily manipulated in the range of the sphere sizes, which are typically 100 nm to 50 nm in diameter. Even smaller spheres (20 nm) can be prepared and used to template small-pore materials. Macrostructured films displaying pore diameters of a few hundred nanometers similar to the wavelength of visible light are promising as photonic crystals [21] exhibiting unique optical properties. The emission of light through a photonic crystal can be manipulated in the region of the photonic bandgap. Photonic materials are being investigated for their potential optical communication and computation applications, with much focus on the design and preparation of three-dimensional structures [22]. Therefore, the ability to engineer porosity on the meso- and macroscales is expected to lead to advanced materials with unique and remarkable properties for a wide variety of emerging nanotechnological applications.

TiO_2 is a very useful semiconducting metal oxide material and exhibits extensive potential applications in catalysis, photocatalysis, sensors, and dye-sensitized solar cells [23]. The photocatalytic activity of TiO_2 is one of its most distinctive features, which is mainly determined by properties involving the crystalline phase, specific surface area, and porous structures. TiO_2 semiconductor had a large direct band gap (3.2 eV), excellent chemical, thermal stability, and other physical properties. Porous nanocrystalline TiO_2 films had been attracted much attention because of their various applications in electronic, electrochemical, photoelectrochemical solar cells [24, 25], electrocatalysts [26], sensors [27], and high-performance photocatalysts [28]. For porous films including TiO_2, various chemical techniques had been employed, such as those based on selective etching [29], self-assembly of block copolymers [30], and close-packed colloidal crystal array templates [31–33]. The processing methods based on the close-packed array templates usually assemble close-packed arrays of monodispersed organic or inorganic spheres (typically polystyrene or silica) as templates by vertical deposition and gravity sedimentation method and then fill the interstices among the closepacked arrays of polystyrene or silica spheres with a precursor, which forms a solid skeleton around the spheres. Finally, a well-defined porous material with narrow pore size distributions can be obtained when the templates are removed either by heat treatment or dissolution with a solvent.

In this paper, based on steady-state fluorescence (SSF) and UVV data and AFM micrographs the effect of annealing temperature, film thickness, and TiO_2 content on the structure and film formation properties of PS/TiO_2 films have been investigated. Based on our previous works [34, 35], films were covered with various layers of TiO_2 using a dip-coating method. Two different sets of films (5 μm and 20 μm) were prepared and annealed at elevated temperatures ranging from 100°C to 280°C. To monitor the film formation stages, fluorescence (I_P) and transmitted light (I_{tr}) intensities were measured after each annealing step. Results showed that film formation process occurred independent of TiO_2 content for all film samples. AFM images show that there is a closely related morphology with the TiO_2 content and film thickness. After removal of PS, thin films gave highly ordered

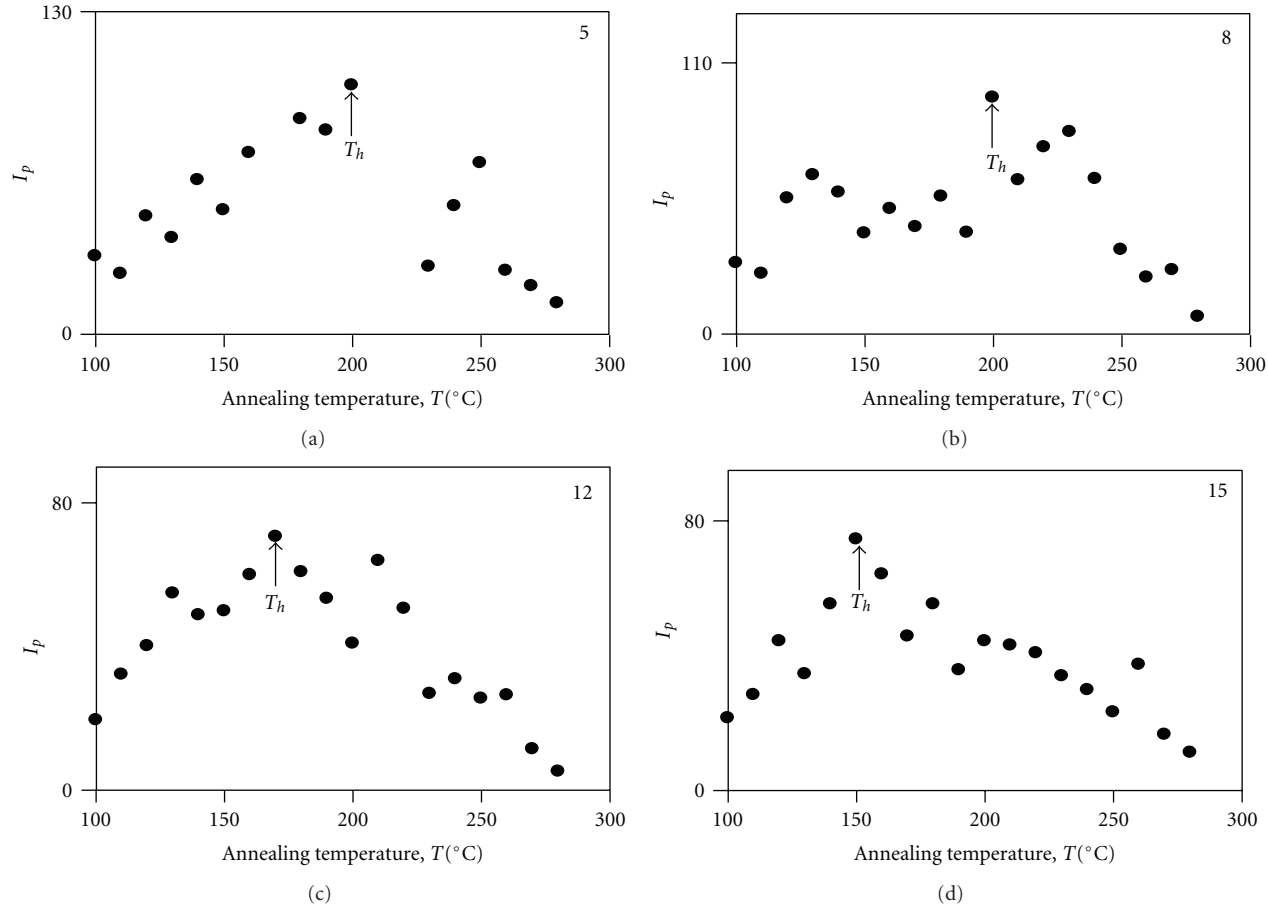

FIGURE 2: Plot of fluorescence intensities, I_P versus annealing temperature, T for the thick composite films for various TiO_2 layers. Numbers on each curve show TiO_2 layer and T_h is the healing temperature.

porous TiO_2 films. However, porous structure cannot be obtained for thick films.

2. Experimental

2.1. Materials

2.1.1. Preparation of Latex Dispersions. Noncrosslinked, Pyrene-(P-) labeled polystyrene (PS) latexes were synthesized by using surfactant free radical emulsion polymerization technique [36]. The polymerization was conducted in 50-mL reactor, using ionized water (50 mL) and distilled styrene (5 g, total amount, 99% pure from Janssen). 1-Pyrenylmethyl methacrylate (0.014 g) (PolyFluoTM 394 from Polyscience) was used as such, and water soluble radical initiator potassium persulfate (KPS) (0.2 g) was used as received. The fluorescent monomer was solubilized in 1 g styrene, and KPS was dissolved in 3 mL water before use. The polymerization was conducted under 300 rpm agitation, nitrogen atmosphere at 90°C during 1 h, and then at 70°C during 16 h. The resulting latex spheres were remained suspended in their mother liquor until needed. These particles have a $T_g = 105$°C and an average diameter 320 nm (see Figure 1). Particle size and its distribution were determined by atomic force microscopic (AFM) observation. The molecular weight of individual PS chain ($M_w = 8.61 \times 10^4$ g·mol^{-1}) were measured by gel permeation chromatography.

2.1.2. TiO_2 Solution. TiO_2 sol was prepared at room temperature in the following way: 1.2 mL titanium (IV) butoxide was injected slowly in 15 mL ethanol. A few drops of acetic acid were added and stirred for half an hour. Later, 10 mL ethanol was added to this mixture and stirred for 1 h.

2.2. Preparation of PS/TiO_2 Films. TiO_2 sol was filled into the PS templates by dip-coating method. The PS latexes were assembled on clean glass substrates by casting method. Firstly, the glass substrates (0.8 cm × 2.5 cm) were cleaned ultrasonically in acetone and deionized water, respectively. Then, PS templates were prepared from the dispersion of PS particles in water by placing the same number of drops on glass substrates and allowing the water to evaporate at room temperature. In order to evaluate the film formation properties depending on the film thickness, two different sets of PS films with 5 μm and 20 μm thick were prepared. The thickness of the PS templates was controlled by changing the amount of PS latex spheres suspension deposited. These films

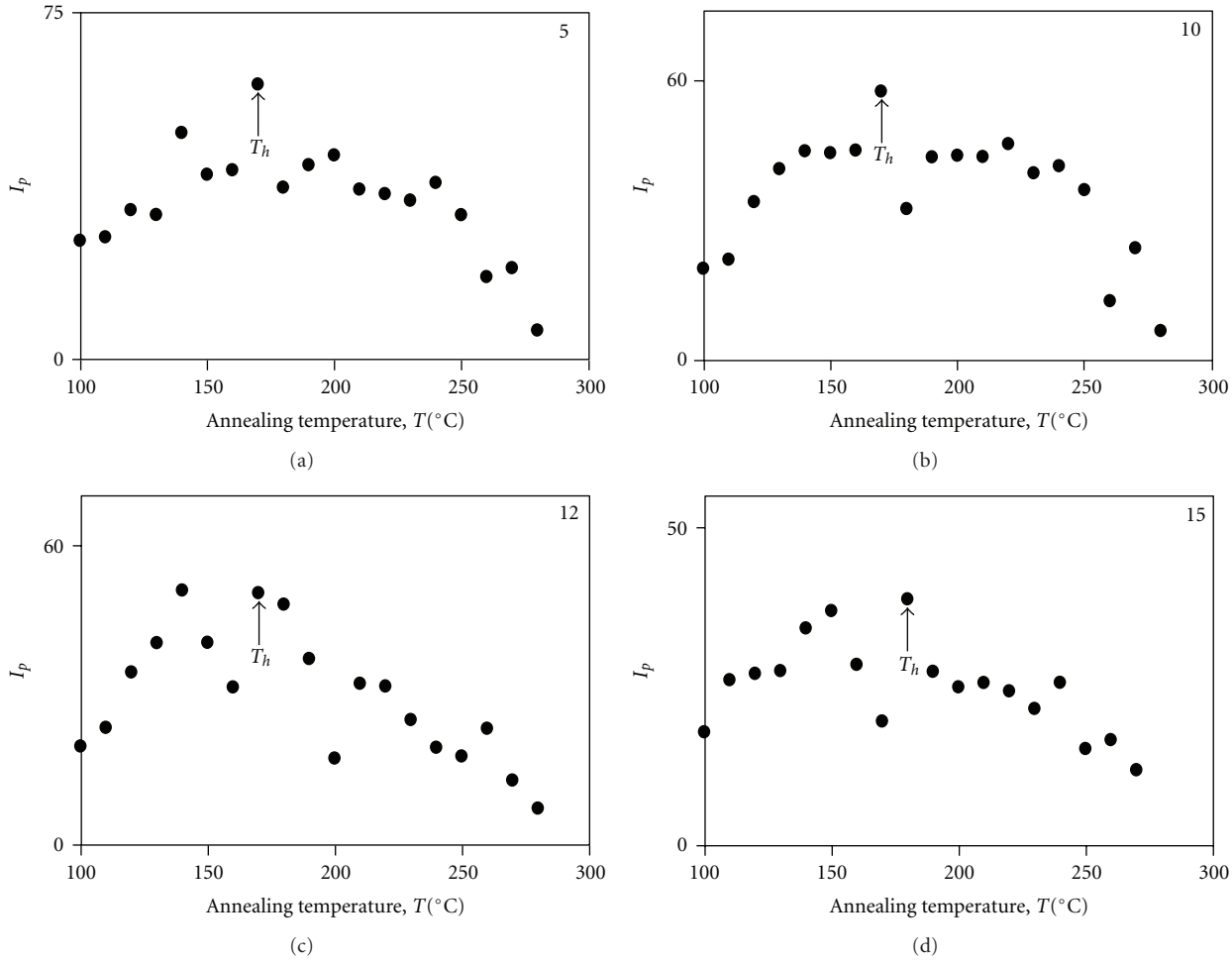

Figure 3: Plot of fluorescence intensities, I_P versus annealing temperature, T for the thin composite films for various TiO_2 layers. Numbers on each curve show TiO_2 layer and T_h is the healing temperature.

then were dipped vertically into TiO_2 sol for several minutes, drawn out and dried at 100°C for 15 min and then the consecutive dipping was performed in order to investigate effect of TiO_2 content. When the templates were immersed into the TiO_2 sol, the TiO_2 precursor could permeate the close-packed arrays of PS by capillary force and form a solid skeleton around the PS spheres. By this method, six different films for each set of films were produced with 5, 8, 10, 12, 13, and 15 layers of TiO_2. Here the TiO_2 content in the films could be adjusted by dipping cycle. The produced films were separately annealed above T_g of PS, 105°C, in 10 min at temperatures ranging from 100 to 280°C. The temperature was maintained within ±2°C during annealing.

After film formation process of PS latexes completed, PS/TiO_2 films were dissolved in toluene for 24 h to remove PS and obtain porous structure of TiO_2 films.

2.3. Methods

2.3.1. Fluorescence Measurements. After annealing, each sample was placed in the solid surface accessory of a Perkin-Elmer Model LS-50 fluorescence spectrometer. Pyrene was excited at 345 nm and fluorescence emission spectra were detected between 360 and 500 nm. All measurements were carried out in the front-face position at room temperature. Slit widths were kept at 8 nm during all SSF measurements.

2.3.2. Photon Transmission Measurements. Photon transmission experiments were carried out using Carry-100 Bio UV-Visible (UVV) scanning spectrometer. The transmittances of the films were detected at 500 nm. A glass plate was used as a standard for all UVV experiments, and measurements were carried out at room temperature after each annealing processes.

2.3.3. Atomic Force Microscopy (AFM) Measurements. Micrographs of the composite films were recorded with a SPM-9500-J3 Shimadzu scanning probe atomic force microscope (AFM). The scan range was chosen between $5 \times 5\,\mu m^2$ to achieve a high resolution. Figure 1 presents the AFM micrograph of PS latex used in this study which shows that the PS spheres are arranged in a close-packed fashion.

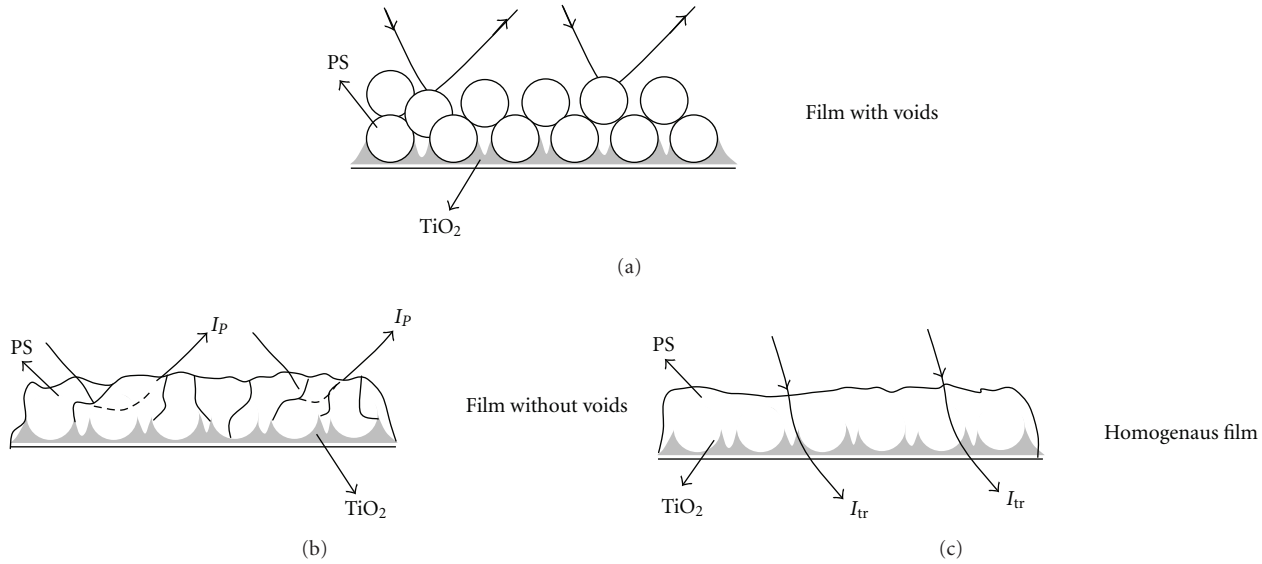

Figure 4: Cartoon representation of the composite films with TiO_2 at several annealing steps: (a) film possesses many voids that results in very low I_P, (b) interparticle voids disappear due to annealing, I_P reaches its maximum value, and (c) transparent film with no voids but some TiO_2 background and has low I_P.

3. Results and Discussions

Fluorescence intensity (I_P) curves of thick and thin PS/TiO_2 composite films for various TiO_2 layers annealed at various temperatures are shown in Figures 2 and 3, respectively. It is clear that the I_P intensity of both sets of film first increases gradually with the increasing annealing temperature up to a certain temperature called healing temperature (T_h), then decreases above this temperature. The increasing annealing temperature up to T_h first causes void closure process due to the viscous flow of PS chains in the latex particles into the interparticle voids, and then further annealing above T_h causes interdiffusion of PS chains across the particle-particles interfaces. The increase and decrease of I_P upon annealing of these composite films can be explained with the void closure and interdiffusion processes, respectively [37, 38]. The behavior of I_P during annealing is schematically presented in Figure 4 for a film with TiO_2 [34, 35, 39]. In Figure 4(a), film possesses many voids, which results in short mean-free and optical paths of a photon yielding very low I_P. Figure 4(b) shows a film in which interparticle voids disappear due to annealing, which gives rise to a long mean free and optical path in the film. At this stage, I_P reaches its maximum values. Finally, Figure 4(c) presents almost transparent film with no voids but some TiO_2 background. At this stage, film has low I_P because the mean free path is very long but the optical path is short.

Figures 5 and 6 show the optical transmittances, I_{tr} (%) of the composite films with various TiO_2 layers annealed at different temperatures from 100°C to 280°C. With the increasing annealing temperature the transmittance of thick films gradually increases (Figure 5). The increase in I_{tr} with annealing temperature for thick films primarily due to the closure of voids [39] between PS particles by viscous flow in these films. Since higher I_{tr} corresponds to higher clarity of the composite, then increase in I_{tr} thick films predicts that microstructure of these films change considerably by annealing them, that is, the transparency of these films evolves upon annealing. PS starts to flow due to annealing, and voids between particles can be filled due to the viscous flow. Further annealing at higher temperatures causes healing and interdiffusion processes, resulting in a more transparent film. There exist two major factors to affect the transmittance, that is, surface scattering and (PS-PS and PS-TiO_2) boundary scattering. Before annealing, since the film contains many voids (i.e., the high number of polymer-air boundaries) most of the light is scattered at the air-polymer interface (surface scattering). After the void closure process is completed, scattering takes place predominantly from the PS-PS and PS-TiO_2 boundaries. However, for thin films I_{tr} almost does not change (see Figure 6) with annealing temperature by predicting that microstructure of thin composites films shows almost no change.

On the other hand, Figure 7 presents the plots of the maximum values of I_{tr}, $(I_{tr})_m$ at 280°C versus number of TiO_2 layers for both sets of films. It is seen that as the number of TiO_2 layer is increased, $(I_{tr})_m$ decreased, indicating that low transparency occurs at higher TiO_2 content for all film samples. Both the thick and thin films annealed at 280°C are shown in Figures 7(a) and 7(b), where the optical transmittance decreased by ~70–60% with increasing TiO_2 layers. This indicates that increase of TiO_2 content, increases the interface scattering which results in the decrease of transmission. This decrease may be attributed to the increasing cluster size and the increasing roughness of the films.

Figures 8, 9, 10, and 11 parts present three-dimensional AFM surface height morphologies of thick and thin PS/TiO_2 composite films with 5, 8, and 12 TiO_2 layer, annealed

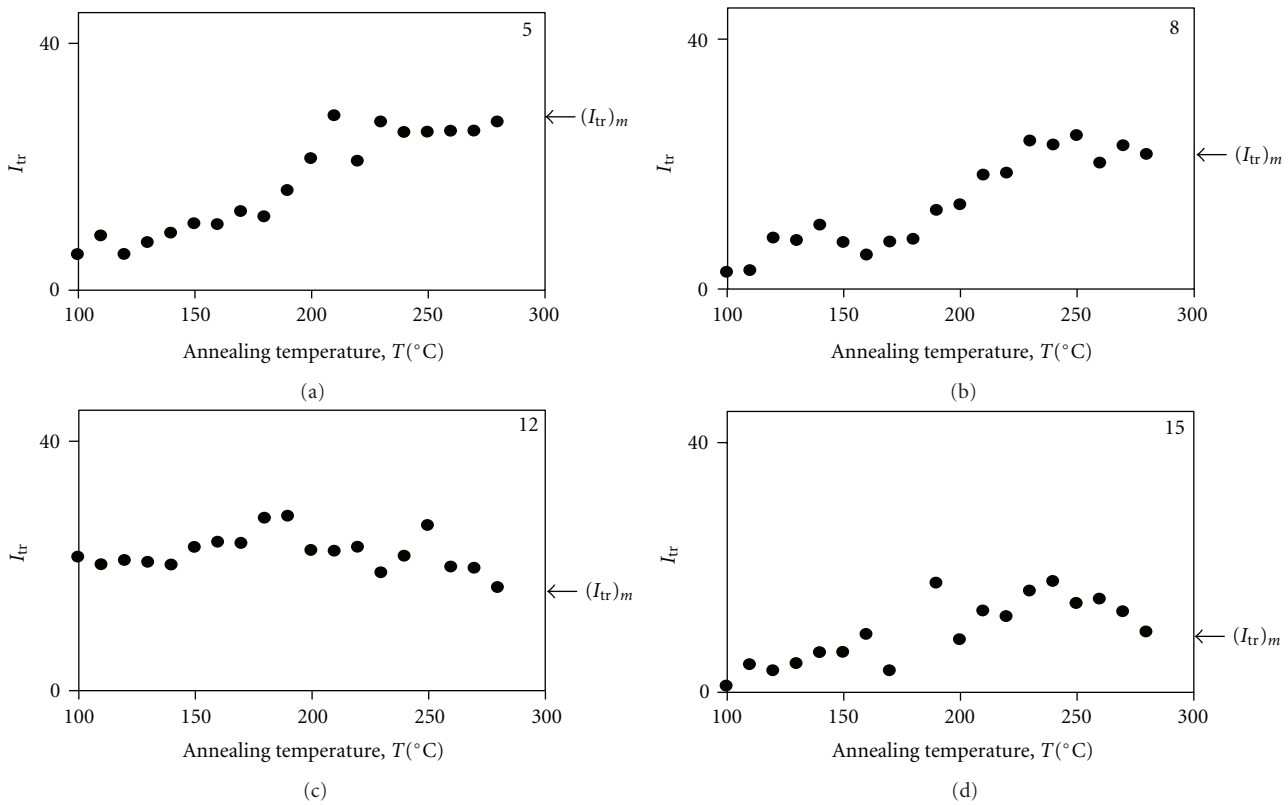

FIGURE 5: Optical transmittance, I_{tr} (%) versus annealing temperatures, T for the thick composite films with various TiO_2 layers. Numbers on each curve show TiO_2 content.

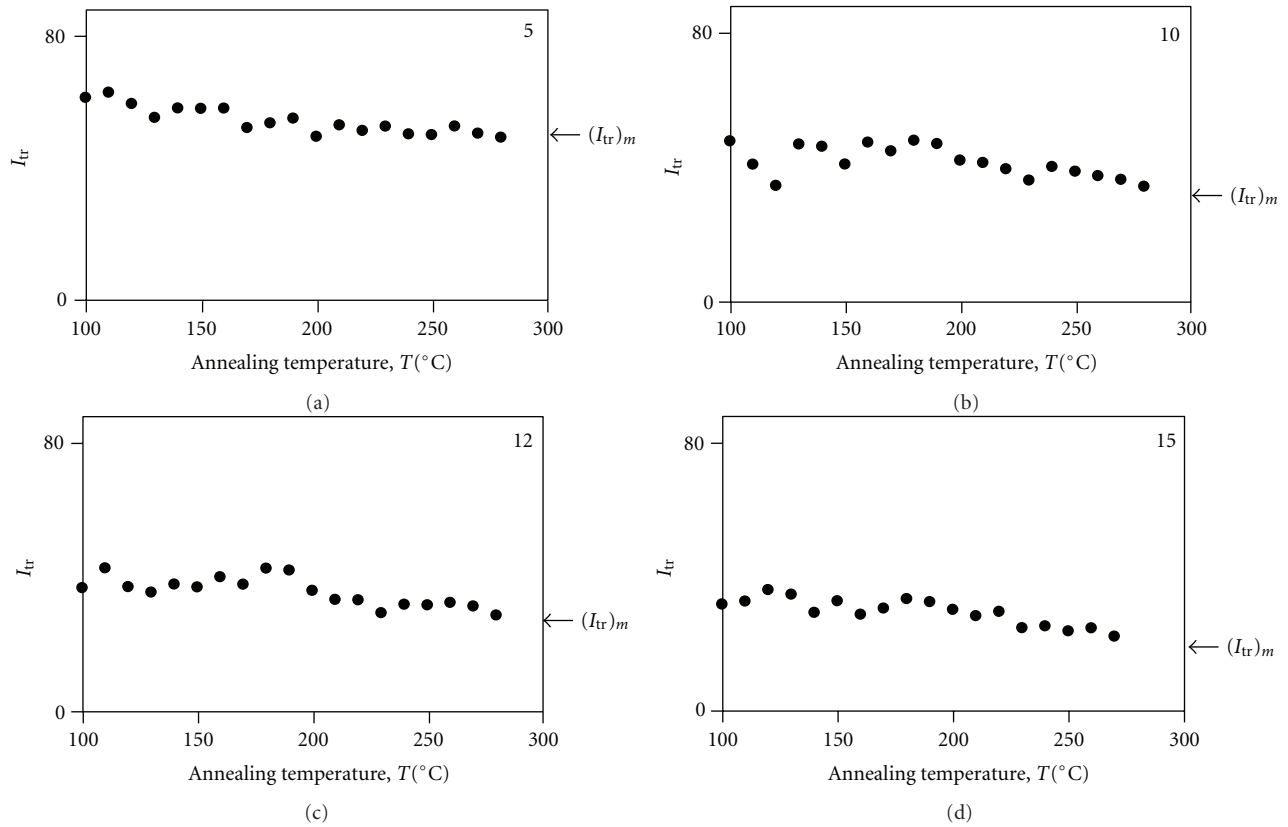

FIGURE 6: Optical transmittance, I_{tr}(%) versus annealing temperatures, T for the thin composite films with various TiO_2 layers. Numbers on each curve show TiO_2 content.

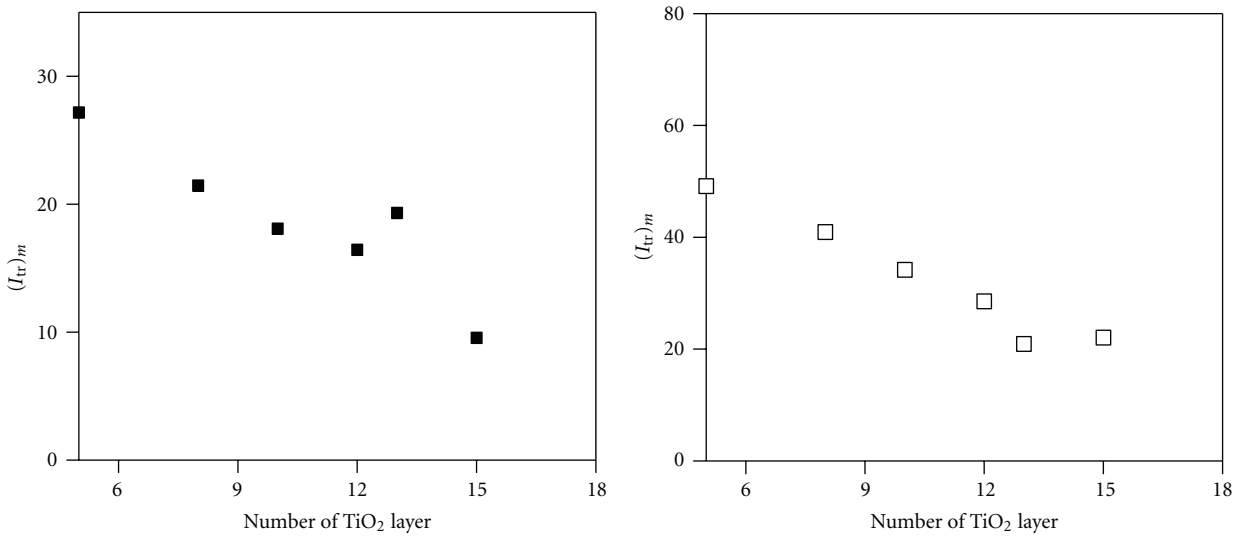

FIGURE 7: Plot of the maxima of transmitted light intensities, $(I_{tr})_m$ from Figures 5 and 6 versus TiO_2 layers for (a) thick and (b) thin composite films.

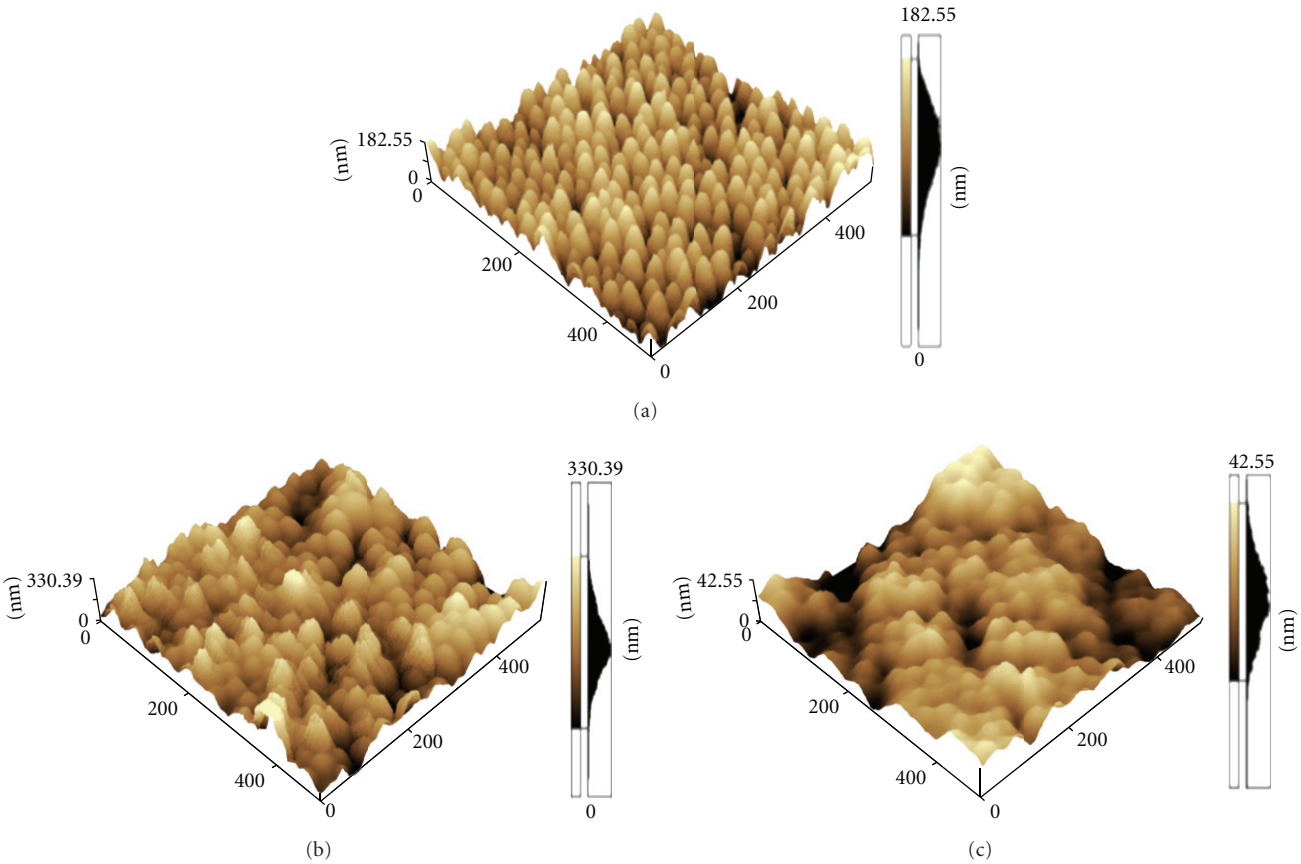

FIGURE 8: AFM images of thick PS/TiO_2 films with (a) 5, (b) 8, and (c) 12 TiO_2 layer annealed at 100°C.

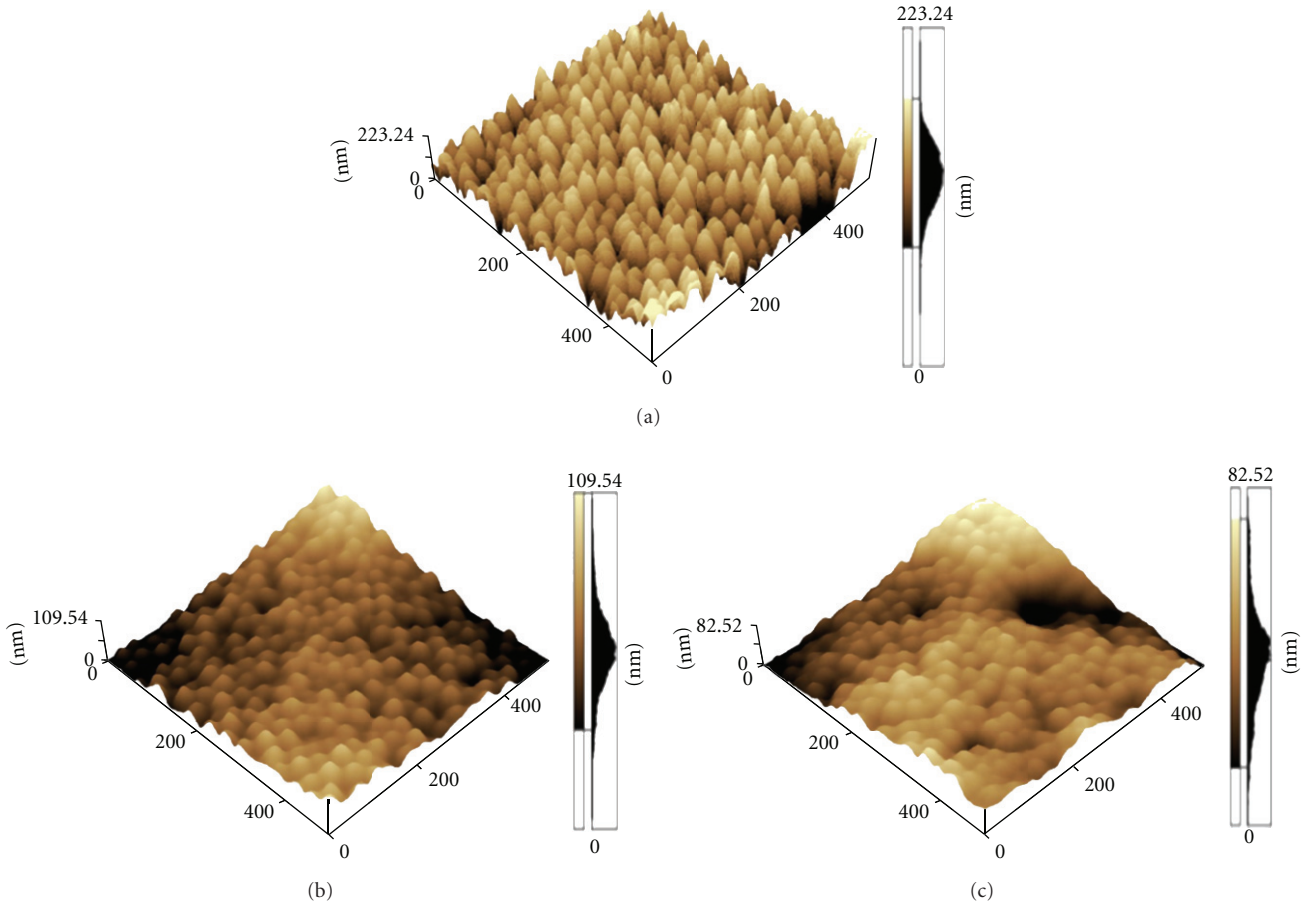

FIGURE 9: AFM images of thin PS/TiO_2 films with (a) 5, (b) 8, and (c) 12 TiO_2 layer annealed at 100°C.

at 100°C and 280°C, respectively. The scanning area is 5 μm × 5 μm. At the right side of the each image, an intensity strip is shown, indicating the depth and height along the z-axis. From these images, it can be seen that the surface of thin composite films is relatively smoother and more regular; thus the surface scattering and boundary scattering of thin films are weaker inducing a rather good transmittance than thick films at all temperatures (see Figure 6). Therefore, annealing the thin films causes no considerable change in the transmittance, whereas AFM images show that the surface roughness of the thick films is decreased with increasing the annealing temperature from 100°C to 280°C which is in agreement with the result of optical transmittance (see Figure 5). In addition, comparing with thin composite films, the cluster sizes of thick films are more nonuniform, and irregular with increasing TiO_2 content which causes a reduction in transmittance. The transmittance of thick films is lower than thin films with increasing TiO_2 content (see Figure 7) at all temperatures as confirmed by AFM images. Nevertheless, from the AFM images of composite films at 280°C, the shape of PS particles is almost destroyed and the microstructure of the latex has disappeared completely, indicating that the interdiffusion of polymer chains has taken place for both sets of films.

Figures 12 and 13 show the influence of TiO_2 concentration and thickness of PS templates on the morphology of porous TiO_2 films after removal of PS templates. For thick films dissolved in toluene (Figure 12), it is seen that microstructure of the thick composite films remain almost unchanged even after dissolution takes place, it still keeps its original microstructure form indicating that PS latex in thick film is highly covered by TiO_2. It can also be seen that porous TiO_2 structure cannot be obtained for these films. However, as shown in Figure 13(a), the porous structure for thin film has primarily been formed for 5 layers of TiO_2. The holes in Figure 13(a) present the places previously occupied by PS latex before dissolution. This behavior can be explained by washing of PS from the surface of the TiO_2 covered latex particles during the dissolution process. In other words, the film formation from PS particles has occurred on top of the TiO_2 covered PS particles during annealing and, during dissolution, PS material is completely dissolved showing the microstructure of PS particles covered by TiO_2 layer. In fact, some of the PS particles are dissolved from the interior of the TiO_2 shell at the bottom of the composite film. However, most of the PS latexes are covered in the rest of the bottom layer. The cartoon presentation in Figure 4(b) coincides with the picture in Figure 13(a), after removal of PS. From the

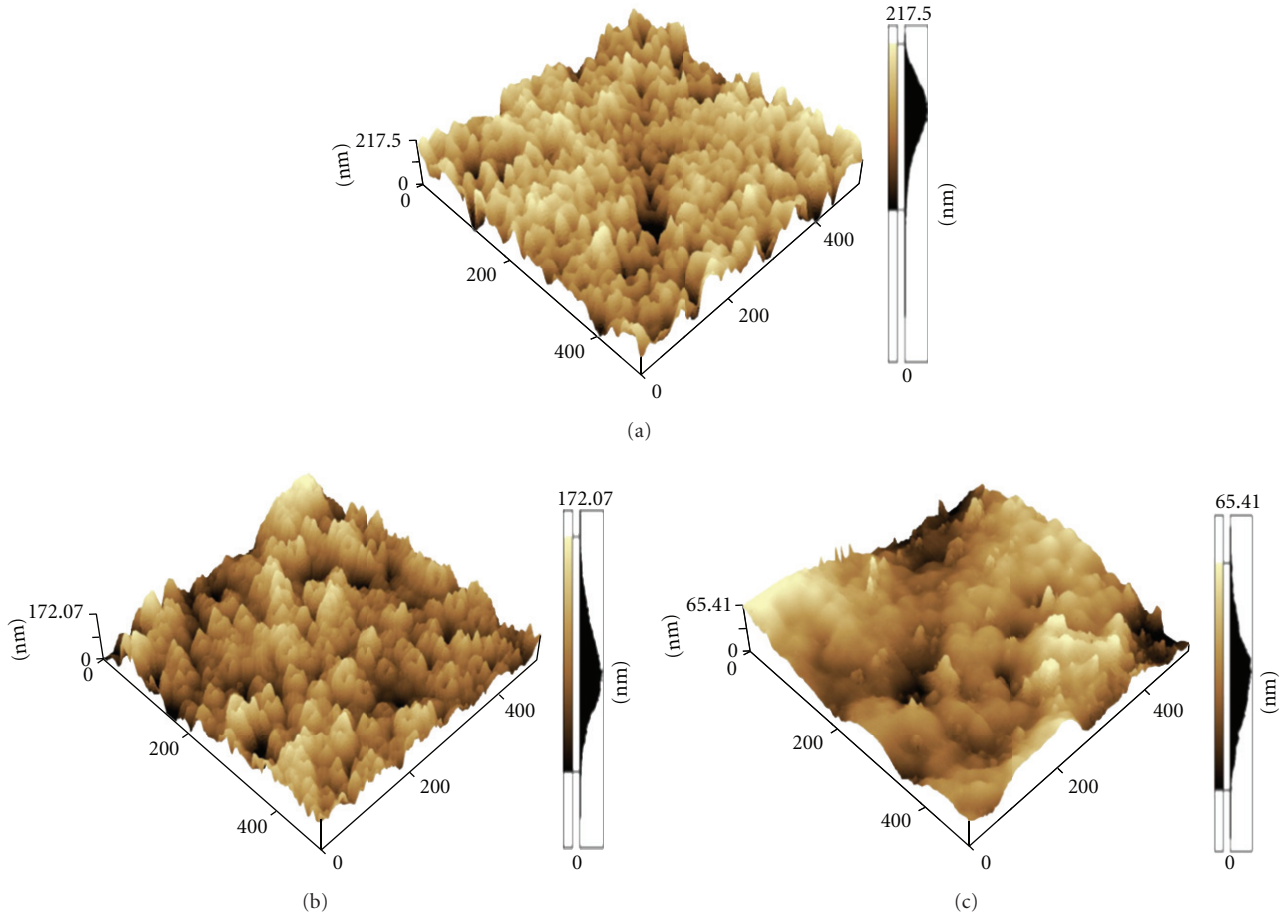

Figure 10: AFM images of thick PS/TiO_2 films with (a) 5, (b) 8, and (c) 12 TiO_2 layer annealed at 280°C.

morphology of thin films with 8 and 12 layers of TiO_2 (Figures 13(b) and 13(c)), it can be seen that a rather flat surface structure appears and porous TiO_2 structure cannot be obtained after dissolution for these films. It is obvious that higher concentration of TiO_2 (the increase of dipping cycles) results in poor permeation among the close-packed arrays of PS for both thick and thin films.

It is understood that both TiO_2 concentration and PS film thickness play an important role in the formation of ordered porous TiO_2 films. No porous structure was seen for the thick PS templates at all TiO_2 concentrations used in this study. On the contrary, it seems that it is easy to fill the interstices of thin PS templates at lower TiO_2 content but it is difficult to fill the interstices at higher TiO_2 concentration. So the TiO_2 content and film thickness are key parameters for the permeation of PS templates. In this experiment, to obtain a porous structure, the suitable thickness of PS templates is 5 μm and TiO_2 content is 5 layers to bring satisfactory permeation to fill the close-packed array of PS templates.

3.1. Film Formation Mechanisms

3.1.1. Void Closure. In order to quantify the behavior of I_P in Figures 2 and 3 below its maxima and I_{tr} in Figure 4, a phenomenological void closure model can be introduced. Latex deformation and void closure between particles can be induced by shearing stress which is generated by surface tension of the polymer, that is, polymer-air interfacial tension. The void closure kinetics can determine the time for optical transparency and latex film formation [40]. In order to relate the shrinkage of spherical void of radius, r, to the viscosity of the surrounding medium, η, an expression was derived and given by the following relation [40]:

$$\frac{dr}{dt} = -\frac{\gamma}{2\eta}\left(\frac{1}{\rho(r)}\right), \tag{1}$$

where γ is the surface energy, t is time, and $\rho(r)$ is the relative density. It has to be noted that here the surface energy causes a decrease in void size, and the term $\rho(r)$ varies with the microstructural characteristics of the material, such as the number of voids, the initial particle size and packing. Equation (1) is similar to one that was used to explain the time dependence of the minimum film formation temperature during latex film formation [41, 42]. If the viscosity is constant in time, integration of (1) gives the relation as

$$t = -\frac{2\eta}{\gamma}\int_{r_0}^{r}\rho(r)dr, \tag{2}$$

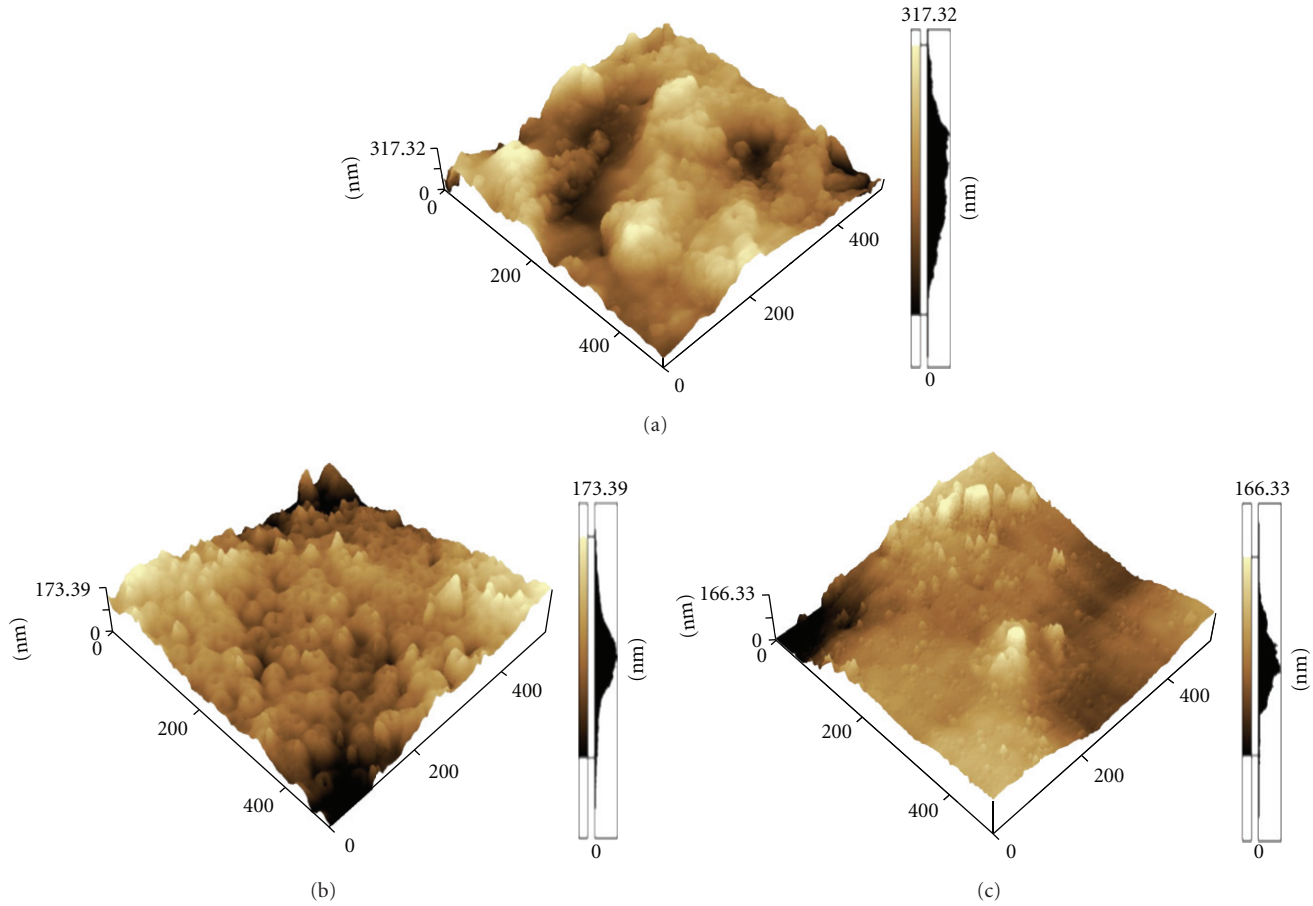

Figure 11: AFM images of thin PS/TiO_2 films with (a) 5, (b) 8, and (c) 12 TiO_2 layer annealed at 280°C.

where r_0 is the initial void radius at time $t = 0$. The dependence of the viscosity of polymer melt on temperature is affected by the overcoming of the forces of macromolecular interaction, which enables the segments of polymer chain to jump over from one equilibration position to another. This process happens at temperatures at which the free volume becomes large enough and is connected with the overcoming of the potential barrier. Frenkel-Eyring theory produces the following relation for the temperature dependence of viscosity [43, 44]

$$\eta = \frac{N_0 h}{V} \exp\left(\frac{\Delta G}{kT}\right), \tag{3}$$

where N_0 is Avogadro's number, h is Planck's constant, V is molar volume, and k is Boltzmann's constant. It is known that $\Delta G = \Delta H - T\Delta S$, so (3) can be written as

$$\eta = A \exp\left(\frac{\Delta H}{kT}\right), \tag{4}$$

where ΔH is the activation energy of viscous flow, that is, the amount of heat which must be given to one mole of material to create the act of a jump during viscous flow; ΔS is the entropy of activation of viscous flow. Here A represents a constant for the related parameters that do not depend on temperature. Combining (2) and (4), the following useful equation is obtained:

$$t = -\frac{2A}{\gamma} \exp\left(\frac{\Delta H}{kT}\right) \int_{r_0}^{r} \rho(r) dr. \tag{5}$$

In order to quantify the above results, (5) can be employed by assuming that the interparticle voids are equal in size and the number of voids stays constant during film formation (i.e. $\rho(r) \approx r^{-3}$). Then integration of (5) gives the relation

$$t = \frac{2AC}{\gamma} \exp\left(\frac{\Delta H}{kT}\right) \left(\frac{1}{r^2} - \frac{1}{r_0^2}\right), \tag{6}$$

where C is a constant related to relative density $\rho(r)$. As we stated before, decrease in void size (r) causes an increase in I_P. If the assumption is made that I_P is inversely proportional to the 6th power of void radius, r, then (6) can be written as

$$t = \frac{2AC}{\gamma} \exp\left(\frac{\Delta H}{kT}\right) \left(I^{1/3}\right). \tag{7}$$

Here, r_0^{-2} is omitted from the relation since it is very small compared to r^{-2} values after void closure processes is started. Equation (4) can be solved for I_P and I_{tr} ($= I$) to interpret the results in Figures 2, 3, and 5 as

$$I(T) = S(t) \exp\left(-\frac{3\Delta H}{kT}\right), \tag{8}$$

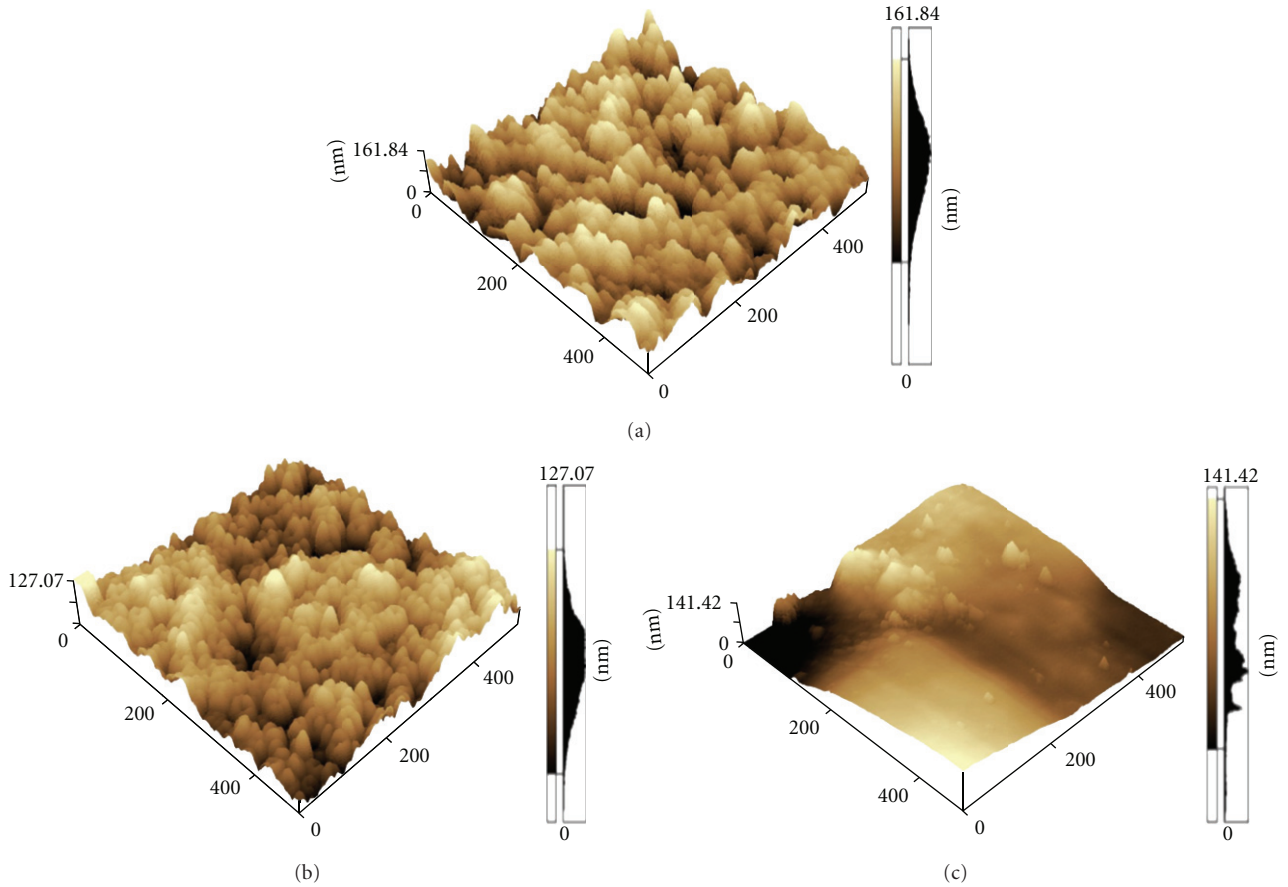

Figure 12: AFM images of the thick PS/TiO_2 films with (a) 5, (b) 8, and (c) 12 TiO_2 layer after removal of the PS overlayer with toluene.

where $S(t) = (\gamma t/2AC)^3$. For a given time the logarithmic form of (5) can be written as follows

$$\ln I(T) = \ln S(t) - \left(\frac{3\Delta H}{kT}\right). \tag{9}$$

As it was already argued above that the increase in both I_P and I_{tr} (for thick films) originate due to the void closure process, then (9) was applied to I_P below maxima (below T_h) and I_{tr} for all film samples in two series. Figures 14 and 15 present the $\ln I_P$ versus T^{-1} and Figure 16 presents $\ln I_{tr}$ versus T^{-1} plots from which ΔH_P and ΔH_{tr} activation energies were obtained. The measured ΔH_P and ΔH_{tr} activation energies are listed in Table 1 for both series. It is seen that activation energies do not change much indicating that the amount of heat that was required by one mole of polymeric material to accomplish a jump during viscous flow does not change by varying the layers on the latex films and latex film thickness. ΔH_P values were found to be smaller than ΔH_{tr} values for both series. This difference most probably originates from different measurement techniques, where the first one is related to the latexes at the surface; however, second one measures the film formation from the inner latexes, which requires higher energies. When comparing the activation energies of both series, it is seen that average ΔH value of thin films is slightly larger than that of thick films. This implies that the viscous flow process is not significantly affected by both TiO_2 content and the thickness of PS template. If one compares the ΔH_P values produced in this study with the values produced for pure PS latex system (ΔH_P = 8.85 kcal·mol^{-1}) [37], then, one can reach a conclusion that inclusion of TiO_2 into the latex system considerably lowers the viscous flow activation energy. In other words, the existence of TiO_2 promotes the void closure process. As a result, latex film formation can be accomplished with much less energy in composites than in a pure latex system. In addition, the produced ΔH_P values in this study are also smaller than the value (ΔH_P = 6.15 kcal/mol) produced in our previous study for PS/TiO_2 films with 1–5 TiO_2 layers [34]. This difference can be explained with higher TiO_2 content in the present study which prevents PS latex to flow.

3.1.2. Healing and Interdiffusion. The decrease in I_P was already explained in previous section, by interdiffusion of polymer chains. As the annealing temperature is increased above maxima, some part of the polymer chains may cross the junction surface and particle boundaries disappear, as a result I_P decreases due to transparency of the film. In order to quantify these results, the Prager-Tirrell (PT) model [45, 46] for the chain crossing density can be employed. These authors used de Gennes's "reptation" model to explain configurational relaxation at the polymer-polymer junction

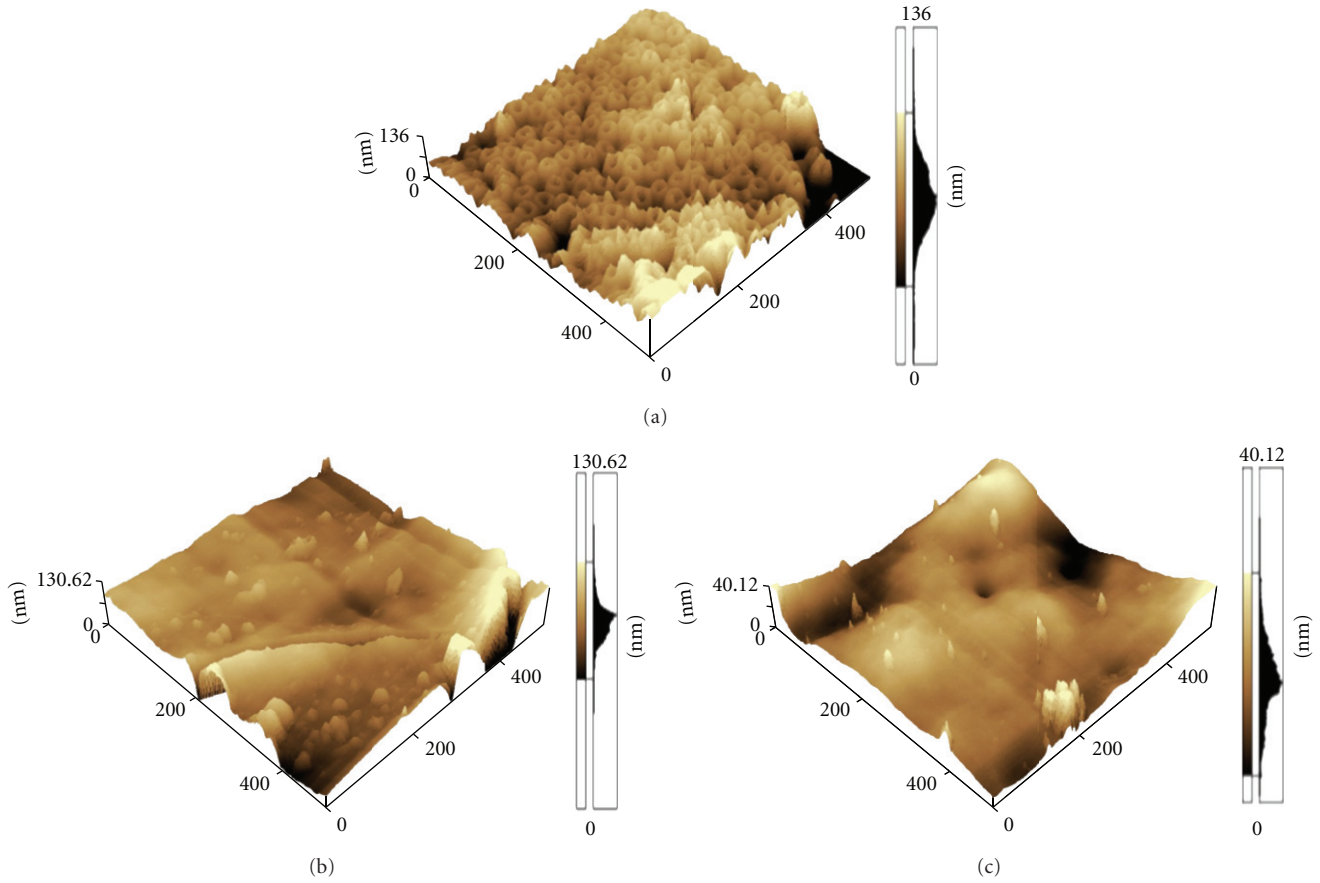

Figure 13: AFM images of the thin PS/TiO_2 films with (a) 5, (b) 8, and (c) 12 TiO_2 layer after removal of the PS overlayer with toluene.

where each polymer chain is considered to be confined to a tube which executes a random back and forth motion [47]. The total "crossing density" $\sigma(t)$ (chains per unit area) at junction surface then was calculated from the contributions $\sigma_1(t)$ due to chains still retaining some portion of their initial tubes, plus a remainder $\sigma_2(t)$, that is, contribution comes from chains which have relaxed at least once. In terms of reduced time $\tau = 2\upsilon t/N^2$ the total crossing density can be written as [48]

$$\frac{\sigma(\tau)}{\sigma(\infty)} = 2\pi^{-1/2}\tau^{1/2}, \tag{10}$$

where υ and N are the diffusion coefficient and number of freely jointed segment of polymer chain [45].

In order to compare our results with the crossing density of the PT model, the temperature dependence of $\sigma(\tau)/\sigma(\infty)$ can be modeled by taking into account the following Arrhenius relation for the linear diffusion coefficient.

$$\upsilon = \upsilon \exp\left(\frac{-\Delta E}{kT}\right). \tag{11}$$

Here ΔE is defined as the activation energy for backbone motion depending on the temperature interval. Combining (10) and (11) a useful relation is obtained as

$$\frac{\sigma(\tau)}{\sigma(\infty)} = R_0 \exp\left(\frac{-\Delta E}{2kT}\right), \tag{12}$$

where $R_0 = (8\upsilon_0 t/\pi N^2)^{1/2}$ is a temperature independent coefficient. The decrease in I_P in Figures 2 and 3 above T_h is already related to the disappearance of particle-particle interface. As annealing temperature increased, more chains relaxed across the junction surface and as a result the crossing density increases. Now, it can be assumed that I_P is inversely proportional to the crossing density $\sigma(T)$ and then the phenomenological equation can be written as

$$I_P(\infty) = R_0^{-1} \exp\left(\frac{\Delta E}{2k_B T}\right). \tag{13}$$

The activation energy of backbone motion; ΔE is produced by fitting the data in Figures 14 and 15 (the left hand side) to (13) and are listed in Table 1. ΔE values also seem not to change by increasing TiO_2 content for both series indicating that TiO_2 content does not affect the backbone motion of the polymer chains across the junction surfaces. In addition, ΔE values are larger than the void closure activation energies for both series. This result is understandable because a single chain needs more energy to execute diffusion across the polymer-polymer interface than to be accomplished by the viscous flow process. Furthermore, it is seen that average ΔE value for thin films is larger than that of thick films, indicating the energy need for the polymer chain is much less in thick films, due to the local pressure created by the neighbouring chains in the film.

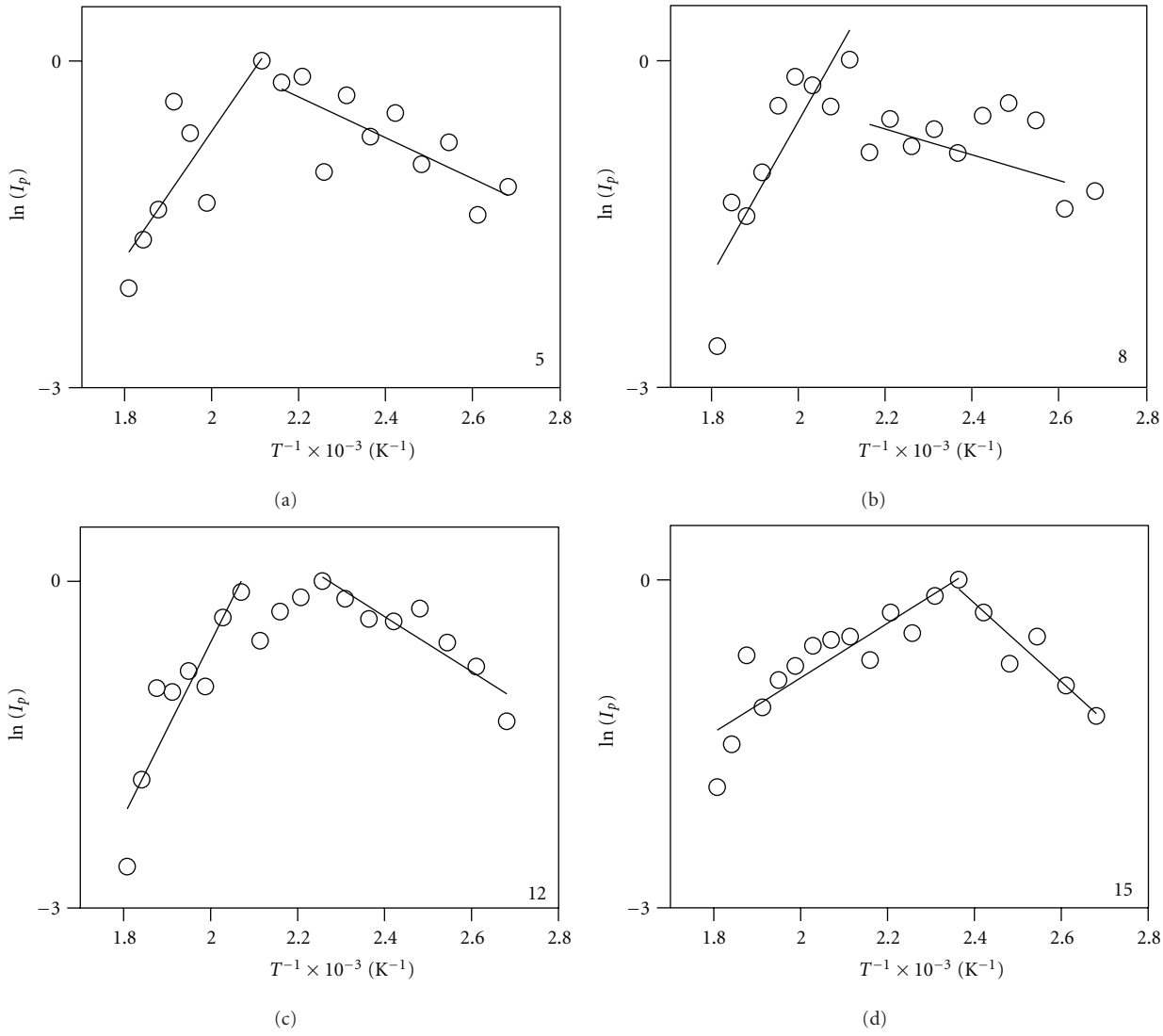

FIGURE 14: The ln(I_P) versus T^{-1} plots of the data in Figure 2 for the thick composite films with 5, 8, 12, and 15 layers of TiO_2. The slope of the straight lines on right and left hand side of the graph produce ΔH_P and ΔE activation energies, respectively.

4. Conclusion

In summary, PS/TiO_2 nanocomposite films with different TiO_2 content on glass substrates were prepared with dip-coating method using thin and thick PS latex templates. Subsequently, TiO_2 sol filled the interstices between the close-packed arrays of PS as the PS templates were dipped into the TiO_2 sol. These films were annealed in the temperature range of 100°C–280°C to monitor the film formation behavior of PS latexes. The results show that both TiO_2 content and PS film thickness played important roles in the film formation behavior and morphology of PS/TiO_2 films. For both sets of films, the classical latex film formation process can take place for all TiO_2 content films on the top surface of the films. From the activation energy values, it has been understood that latex film formation process can be developed independent of TiO_2 content but slightly dependent on the thickness of PS templates. After film formation process completed, a well-defined porous TiO_2 structure was obtained for thin films after removing the PS templates. Whereas, no porous structure was seen for the thick PS templates at all TiO_2 content. In this experiment, it seems that the suitable thickness of PS templates is 5 μm and TiO_2 content is 5 layer of TiO_2 to bring satisfactory permeation to fill the close-packed array of PS templates. These findings provide insight into the principle mechanism of latex film formation in inorganic oxide-based systems. Therefore, our study presents useful information and ideas about the kinetics of latex film formation in composite systems.

Finally, using a simple, cheap, and environmentally friendly method, we have shown that a quite ordered porous ceramic structure by presenting a replica of the PS particles can be produced. It should be noted that the void diameter depends on the size of PS used and the TiO_2 content. We will investigate the effect of PS size and PS molecular weight on

Table 1: Experimentally produced activation energies for thick and thin films for varying numbers of TiO_2 layers.

TiO_2 layer	Thick films (20 μm)			Thin films (5 μm)		
	ΔH_P (kcal·mol^{-1})	ΔH_{tr} (kcal·mol^{-1})	ΔE (kcal.mol^{-1})	ΔH_P (kcal·mol^{-1})	ΔH_{tr} (kcal·mol^{-1})	ΔE (kcal·mol^{-1})
5	1.24	1.88	23.14	1.20	—	46.14
8	0.51	1.70	27.92	0.31	—	9.35
10	0.30	1.32	12.74	1.60	—	47.54
12	1.68	0.80	31.71	2.51	—	12.94
13	0.90	0.66	23.63	0.91	—	34.6
15	2.38	4.30	9.93	1.35	—	9.90
Average	1.17	1.78	21.51	1.31	—	26.74

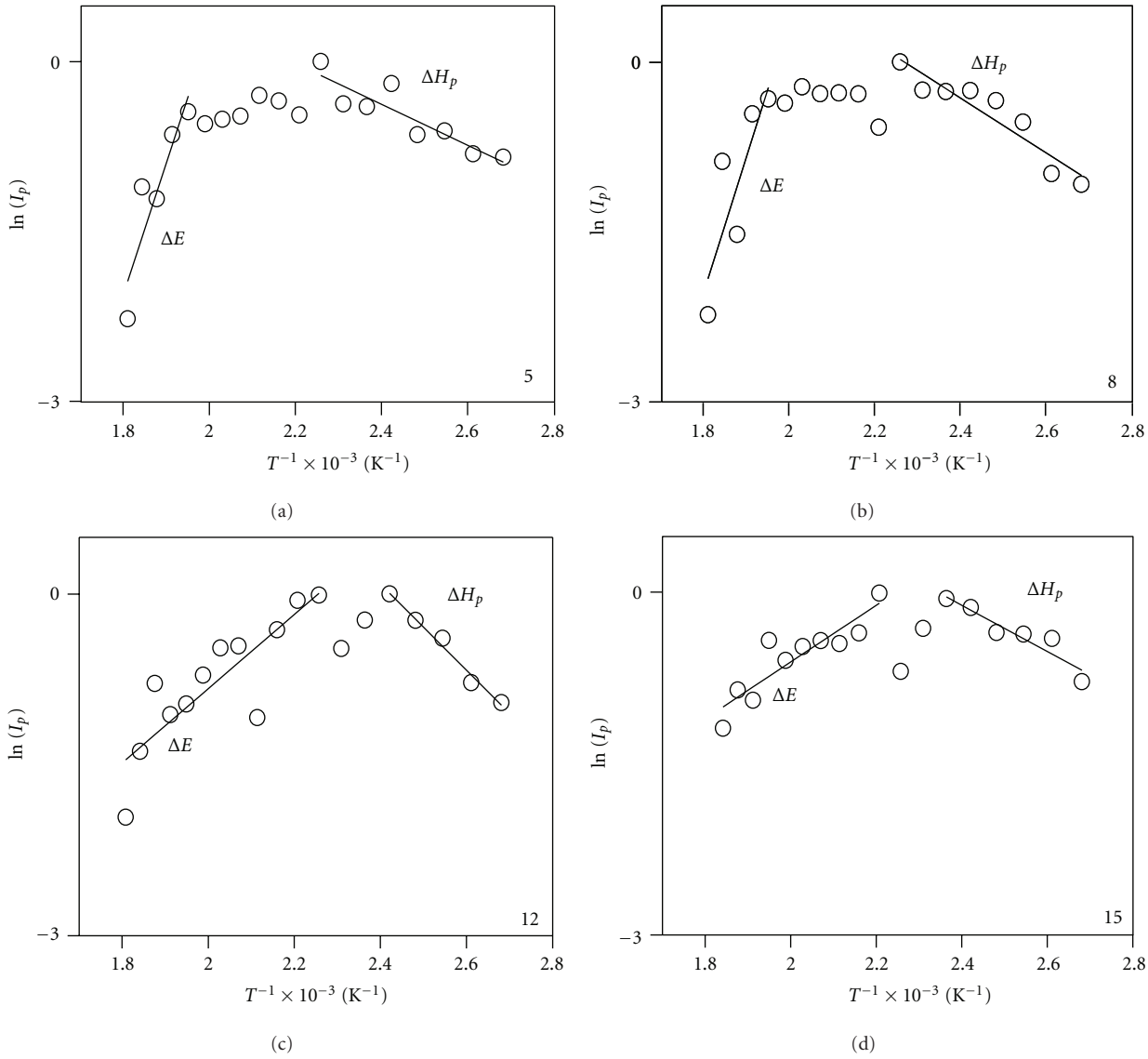

Figure 15: The ln(I_P) versus T^{-1} plots of the data in Figure 3 for the thin composite films with 5, 10, 12, and 15 layers of TiO_2. The slope of the straight lines on right and left hand side of the graph produce ΔH_P and ΔE activation energies, respectively.

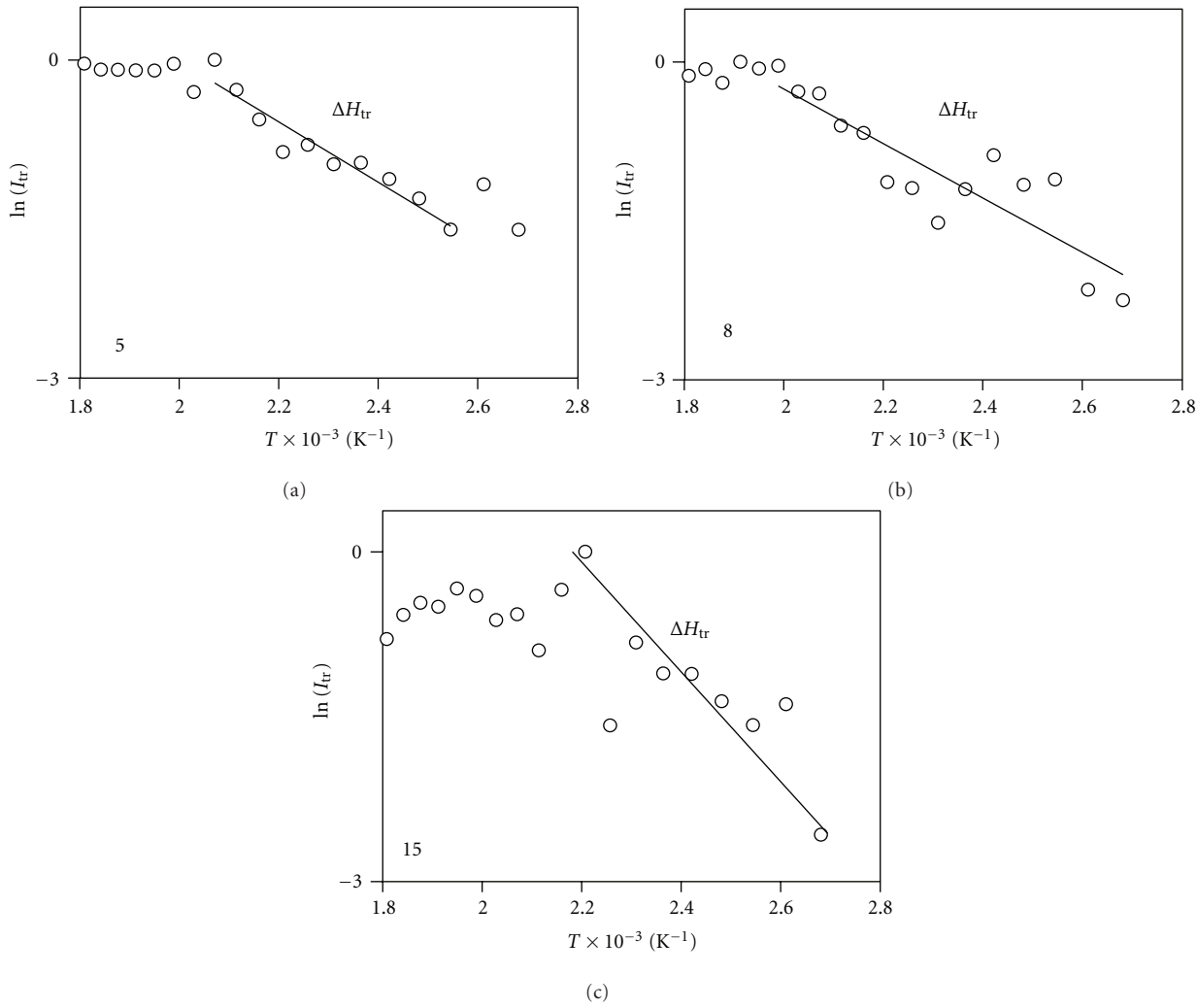

FIGURE 16: The $\ln(I_{tr})$ versus T^{-1} plots of the data in Figure 5 for the thick composite film contains 5, 8, 12, and 15 layers of TiO_2. The slope of the straight lines produces ΔH_{tr}.

film formation and microstructure of PS/TiO_2 composites in future work.

Acknowledgments

One of the authors (O. Pekcan) thanks the Turkish Academy of Sciences (TUBA) for their partial support.

References

[1] T. Provder, M. A. Winnik, and M. W. Urban, *Film Formation in Waterborne Coatings*, ACS Symposium Series 648, American Chemical Society, Washington, DC, USA, 1996.

[2] P. R. Sperry, B. S. Snyder, M. L. O'Dowd, and P. M. Lesko, "Role of water in particle deformation and compaction in latex film formation," *Langmuir*, vol. 10, no. 8, pp. 2619–2628, 1994.

[3] J. K. Mackenzie and R. Shuttleworth, "A phenomenological theory of sintering," *Proceedings of the Physical Society B*, vol. 62, no. 12, article 310, pp. 833–852, 1949.

[4] J. L. Keddie, "Film formation of latex," *Materials Science and Engineering R*, vol. 21, no. 3, pp. 101–170, 1997.

[5] J. N. Yoo, L. H. Sperling, C. J. Glinka, and A. Klein, "Characterization of film formation from polystyrene latex particles via SANS. 2. High molecular weight," *Macromolecules*, vol. 24, no. 10, pp. 2868–2876, 1991.

[6] O. Pekcan, "Interdiffusion during latex film formation," *Trends in Polymer Science*, vol. 2, p. 236, 1994.

[7] M. E. Davis, "Ordered porous materials for emerging applications," *Nature*, vol. 417, no. 6891, pp. 813–821, 2002.

[8] X. S. Zhao, "Novel porous materials for emerging applications," *Journal of Materials Chemistry*, vol. 16, pp. 623–625, 2006.

[9] C. T. Kresge, M. E. Leonowicz, W. J. Roth, J. C. Vartuli, and J. S. Beck, "Ordered mesoporous molecular sieves synthesized by a liquid-crystal template mechanism," *Nature*, vol. 359, no. 6397, pp. 710–712, 1992.

[10] G. J. D. A. A. Soler-Illia, C. Sanchez, B. Lebeau, and J. Patarin, "Chemical strategies to design textured materials: from microporous and mesoporous oxides to nanonetworks and hierarchical structures," *Chemical Reviews*, vol. 102, no. 11, pp. 4093–4138, 2002.

[11] M. L. K. Hoa, M. Lu, and Y. Zhang, "Preparation of porous materials with ordered hole structure," *Advances in Colloid and Interface Science*, vol. 121, no. 1–3, pp. 9–23, 2006.

[12] O. D. Velev, T. A. Jede, R. F. Lobo, and A. M. Lenhoff, "Porous silica via colloidal crystallization," *Nature*, vol. 389, no. 6650, pp. 447–448, 1997.

[13] D. Wang, R. A. Caruso, and F. Caruso, "Synthesis of macroporous titania and inorganic compostie materials from coated colloidal spheres—a novel route to tune pore morphology," *Chemical Communications*, vol. 13, pp. 364–371, 2002.

[14] Z. Y. Yuan, J. L. Blin, and B. L. Su, "Design of bimodal mesoporous silicas with interconnected pore systems by ammonia post-hydrothermal treatment in the mild-temperature range," *Chemical Communications*, vol. 5, pp. 504–505, 2002.

[15] P. Yang, T. Deng, D. Zhao et al., "Hierarchically ordered oxides," *Science*, vol. 282, no. 5397, pp. 2244–2246, 1998.

[16] B. T. Holland, L. Abrams, and A. Stein, "Dual templating of macroporous silicates with zeolitic microporous frameworks," *Journal of the American Chemical Society*, vol. 121, no. 17, pp. 4308–4309, 1999.

[17] B. Lebeau, C. E. Fowler, S. Mann, C. Farcet, B. Charleux, and C. Sanchez, "Synthesis of hierarchically ordered dye-functionalised mesoporous silica with macroporous architecture by dual templating," *Journal of Materials Chemistry*, vol. 10, no. 9, pp. 2105–2108, 2000.

[18] B. T. Holland, C. F. Blanford, T. Do, and A. Stein, "Synthesis of highly ordered, three-dimensional, macroporous structures of amorphous or crystalline inorganic oxides, phosphates, and hybrid composites," *Chemistry of Materials*, vol. 11, no. 3, pp. 795–805, 1999.

[19] M. A. Carreon and V. V. Guliants, "Macroporous vanadium phosphorus oxide phases displaying three-dimensional arrays of spherical voids," *Chemistry of Materials*, vol. 14, no. 6, pp. 2670–2675, 2002.

[20] D. Wang, R. A. Caruso, and F. Caruso, "Synthesis of macroporous titania and inorganic composite materials from coated colloidal spheres—a novel route to tune pore morphology," *Chemistry of Materials*, vol. 13, no. 2, pp. 364–371, 2001.

[21] M. E. Turner, T. J. Trentler, and V. L. Colvin, "Thin films of macroporous metal oxides," *Advanced Materials*, vol. 13, no. 3, pp. 180–183, 2001.

[22] D. G. Norris and Y. A. Vlasov, "Chemical approaches to three-dimensional semiconductor photonic crystals," *Advanced Materials*, vol. 13, no. 6, pp. 371–376, 2001.

[23] X. Chen and S. S. Mao, "Titanium dioxide nanomaterials: synthesis, properties, modifications and applications," *Chemical Reviews*, vol. 107, no. 7, pp. 2891–2959, 2007.

[24] B. O'Regan and M. Grätzel, "A low-cost, high-efficiency solar cell based on dye-sensitized colloidal TiO_2 films," *Nature*, vol. 353, no. 6346, pp. 737–740, 1991.

[25] B. O'Regan, D. T. Schwartz, S. M. Zakeeruddin, and M. Grätzel, "Electrodeposited nanocomposite N-P heterojunctions for solid-state dye-sensitized photovoltaics," *Advanced Materials*, vol. 12, no. 17, pp. 1263–1267, 2000.

[26] B. B. Lakshmi, P. K. Dorhout, and C. R. Martin, "Sol-gel template synthesis of semiconductor nanostructures," *Chemistry of Materials*, vol. 9, no. 3, pp. 857–862, 1997.

[27] H. M. Lin, T. Y. Hsu, C. Y. Tung, and C. M. Hsu, "Hydrogen sulfide detection by nanocrystal PT doped TiO_2-based gas sensors," *Nanostructured Materials*, vol. 6, no. 5–8, pp. 1001–1004, 1995.

[28] K. R. Gopidas, M. Bohorquez, and P. V. Kamat, "Photophysical and photochemical aspects of coupled semiconductors. Charge-transfer processes in colloidal CdS-TiO_2 and CdS-AgI systems," *Journal of Physical Chemistry*, vol. 94, no. 16, pp. 6435–6440, 1990.

[29] R. C. Furneaux, W. R. Rigby, and A. P. Davidson, "The formation of controlled-porosity membranes from anodically oxidized aluminium," *Nature*, vol. 337, no. 6203, pp. 147–149, 1989.

[30] G. Widawski, M. Rawiso, and B. Francois, "Self-organized honeycomb morphology of star-polymer polystyrene films," *Nature*, vol. 369, no. 6479, pp. 387–389, 1994.

[31] L. I. Halaoui, N. M. Abrams, and T. E. Mallouk, "Increasing the conversion efficiency of dye-sensitized TiO_2 photoelectrochemical cells by coupling to photonic crystals," *Journal of Physical Chemistry B*, vol. 109, no. 13, pp. 6334–6342, 2005.

[32] P. N. Bartlett, J. J. Baumberg, P. R. Birkin, M. A. Ghanem, and M. C. Netti, "Highly ordered macroporous gold and platinum films formed by electrochemical deposition through templates assembled from submicron diameter monodisperse polystyrene spheres," *Chemistry of Materials*, vol. 14, no. 5, pp. 2199–2208, 2002.

[33] G. Subramanian, V. N. Manoharan, J. D. Thorne, and D. J. Pine, "Ordered macroporous materials by colloidal assembly: a possible route to photonic bandgap materials," *Advanced Materials*, vol. 11, no. 15, pp. 1261–1265, 1999.

[34] S. Ugur, S. Sunay, A. Elaissari, F. Tepehan, and O. Pekcan, "Film formation from nano-sized polystrene latex covered with various TiO_2 layers," *Polymer Composites*, vol. 27, no. 6, pp. 651–659, 2006.

[35] S. Ugur, S. Sunay, F. Tepehan, and O. Pekcan, "Film formation from TiO_2-polystyrene latex composite: a fluorescence study," *Composite Interfaces*, vol. 14, no. 3, pp. 243–260, 2007.

[36] J. S. Liu, J. Feng, and M. A. Winnik, "Study of polymer diffusion across the interface in latex films through direct energy transfer experiments," *Journal of Chemical Physics*, vol. 101, no. 10, pp. 9096–9103, 1994.

[37] S. Ugur, A. Elaissari, and O. Pekcan, "Void closure and interdiffusion processes during latex film formation from surfactant-free polystyrene particles: a fluorescence study," *Journal of Colloid and Interface Science*, vol. 263, no. 2, pp. 674–683, 2003.

[38] S. Ugur, A. Elaissari, and O. Pekcan, "Film formation from surfactant-free, slightly crosslinked, fluorescein-labeled polystyrene particles," *Journal of Coatings Technology Research*, vol. 1, no. 4, pp. 305–313, 2004.

[39] M. Canpolat and O. Pekcan, "Healing and photon diffusion during sintering of high-T latex particles," *Journal of Polymer Science B*, vol. 34, no. 4, pp. 691–698, 1996.

[40] J. L. Keddie, P. Meredith, R. A. L. Jones, and A. M. Donald, "Rate-limiting steps in film formation of acrylic latices as elucidated with ellipsometry and environmental scanning electron microscopy," in *Film Formation in Waterborne Coatings*, T. Provder, M. A. Winnik, and M. W. Urban, Eds., vol. 648 of *ACS Symposium Series*, pp. 332–348, American Chemical Society, Washington, DC, USA, 1996.

[41] G. B. McKenna, "Glass formation and glassy behavior," in *Comprehensive Polymer Science*, C. Booth and C. Price, Eds., vol. 2, pp. 311–362, Pergamon Press, Oxford, UK, 1989.

[42] H. Vogel, "Das Temperaturabhaengigkeitsgesetz der Viskositaet von Fluessigkeiten," *Physikalische Zeitschrift*, vol. 22, pp. 645–646, 1921.

[43] G. S. Fulcher, "Analysis of recent measurements of the viscosity of glasses," *Journal of the American Ceramic Society*, vol. 8, pp. 339–355, 1925.

[44] J. Frenkel, "Viscous flow of crystalline bodies under the action of surface tension," *Journal of Physics*, vol. 9, pp. 385–391, 1945.

[45] S. Prager and M. Tirrell, "The healing process at polymer-polymer interfaces," *Journal of Chemical Physics*, vol. 75, no. 10, pp. 5194–5198, 1981.

[46] R. P. Wool, B. L. Yuan, and O. J. McGarel, "Welding of polymer interfaces," *Polymer Engineering and Science*, vol. 29, no. 19, pp. 1340–1367, 1989.

[47] P. G. de Gennes, "Kinetics of diffusion-controlled processes in dense polymer systems. II. Effects of entanglements," *Journal of Chemical Physics*, vol. 76, no. 6, pp. 3322–3326, 1982.

[48] Ö. Pekcan and E. Arda, "Void closure and interdiffusion in latex film formation by photon transmission and fluorescence methods," *Colloids and Surfaces A*, vol. 153, no. 1–3, pp. 537–549, 1999.